Geophys. J. Int. (2004) **156,** 549–554 doi: 10.1111/j.1365-246X.2004.02133.x

Null-space and statistical significance of first-arrival traveltime inversion

Igor B. Morozov

Department of Geological Sciences, University of Saskatchewan, Saskatoon, SK S7N 5E2, *Canada. E-mail igor.morozov@usask.ca*

Accepted 2003 September 10. Received 2003 July 1; in original form 2002 June 5

SUMMARY

The strong uncertainty inherent in the traveltime inversion of first arrivals from surface sources is usually removed by using *a priori* constraints or regularization. This leads to the null-space (data-independent model variability) being inadequately sampled, and consequently, model uncertainties may be underestimated in traditional (such as checkerboard) resolution tests. To measure the full null-space model uncertainties, we use unconstrained Monte Carlo inversion and examine the statistics of the resulting model ensembles. In an application to 1-D first-arrival traveltime inversion, the τ–p method is used to build a set of models that are equivalent to the IASP91 model within small, ~0.02 per cent, time deviations. The resulting velocity variances are much larger, ~2–3 per cent within the regions above the mantle discontinuities, and are interpreted as being due to the null-space. Depth-variant depth averaging is required for constraining the velocities within meaningful bounds, and the averaging scalelength could also be used as a measure of depth resolution. Velocity variances show structure-dependent, negative correlation with the depth-averaging scalelength. Neither the smoothest (Herglotz–Wiechert) nor the mean velocity-depth functions reproduce the discontinuities in the IASP91 model; however, the discontinuities can be identified by the increased null-space velocity (co-)variances. Although derived for a 1-D case, the above conclusions also relate to higher dimensions.

Key words: first-arrival traveltimes, IASP91, inversion, model uncertainty, Monte Carlo.

INTRODUCTION

The inversion of first-arrival traveltimes is a key element of traveltime analysis that provides information on the velocity structures required for both traveltime interpretation and waveform imaging. However, it is well known that in most realistic cases with surface sources and receivers, inversion of the first arrivals is inherently non-unique (e.g. Aki & Richards 2002, Section 9.4). This non-uniqueness arises from the possibility of low-velocity zones and layers 'hidden' from the first arrivals by the velocities increasing with depth (Healy 1963), the very same property that makes refraction imaging possible. An example of such a layer is the entire lower crust in the IASP91 model that is hidden in the first arrivals by the faster Moho arrival. Certain velocity structures have no expression in the first-arrival traveltimes and thus belong to the null-space of the forward problem (Menke 1989).

As a result of its ray geometry, the null space of surface refraction traveltimes contains large model uncertainties that are significant for interpretation. However, the existing first-arrival inversion methods usually eliminate this null-space by using *a priori* constraints or various types of regularization (e.g. Zelt 1999), and consequently the resulting model variances may be strongly underestimated. Although the *a priori* constraints may be justified in retrospect, by the viability and significance of the resulting interpretations, it is also desirable to assess the model variance and resolution afforded by the traveltime data alone (or at least with minimal constraints). Multivariate, non-linear optimization provides a suitable framework for such assessment (e.g. Pullammanappallil & Louie 1994; Zhang & Toksőz M.N. 1998).

In a form suitable for Monte Carlo analysis, the null-space, $\mathcal{M}_0$, of a general traveltime problem is given by

$$\mathcal{M}_0 = \lim \mathcal{M}(\delta t)|_{\delta t \to 0}, \tag{1}$$

where $\mathcal{M}(\delta t)$ is the set of models having traveltime misfits (measured using an appropriate norm) smaller than δt. In a linear, Gaussian case, the distribution $\mathcal{M}(\delta t)$ can be characterized by the model covariance matrix that is explicitly partitioned into a null-space contribution and a projection of data errors on to the model space (*cf.* Menke 1989, eq. 5.23):

$$[\mathrm{cov}\,\mathbf{m}] = [\mathbf{I} - \mathbf{R}]\,[\mathrm{cov}\ \mathbf{m}^a]\,[\mathbf{I} - \mathbf{R}]^T + \mathbf{G}^{-g}\,[\mathrm{cov}\,\mathbf{t}]\,\mathbf{G}^{-gT}. \tag{2}$$

Here, $\mathrm{cov}\,\mathbf{m}^a$ is the *a priori* model covariance, $\mathrm{cov}\,\mathbf{t}$ is the data (traveltime) covariance, $\mathbf{G}^{-g}$ is the generalized inverse, $\mathbf{R} = \mathbf{G}^{-g}\mathbf{G}$ is the resolution matrix, $\mathbf{G}$ is the forward modelling operator, and T denotes the transpose. Expression (2), however, is not very useful for the unconstrained, non-Gaussian first-arrival inversion for

which $\mathbf{m}^a$ and $\mathbf{G}^{-g}$ are difficult to define meaningfully. Instead, we use Monte Carlo analysis to estimate the null-space directly from the general relation (1), by allowing small (∼0.02 per cent in the following examples) traveltime perturbations, collecting the solutions that belong to $\mathcal{M}(\delta t)$, and measuring the resulting finite (∼2–3 per cent) model variances.

Below, Monte Carlo sampling is used to derive ensembles of models that are practically equivalent to the IASP91 model (Kennett & Engdahl 1991) in terms of their first-arrival traveltimes. The IASP91 model is an ideal example to study the uncertainty of the first-arrival inversion, with the algorithm for accurate traveltime computation available (Buland & Chapman 1983). The resulting near-null space velocity variances are measured and characterized through a model-dependent trade-off between the velocity uncertainty and depth-averaging scalelength. The observed limitations are related to the fundamental properties of the surface first-arrival inversion and should remain valid for 2- and 3-D cases.

MAPPING THE τ–p TRAVELTIMES TO DEPTH

The 'tau' method (Bessonova *et al.* 1974; hereafter referred to as the τ–p method; see also Pavlenkova 1982; Buland & Chapman 1983) provides a convenient framework for 1-D traveltime inversion. The method is based on a representation of the observed traveltime curve as an envelope of a family of linear segments (head-waves) characterized by their ray parameters, p, and intercept times, τ (Fig. 1). For diving waves in a 1-D Earth, the values of τ always increase with decreasing p, and the dependence $\tau(p)$ can be uniquely modelled by a sequence of constant-velocity layers corresponding to the individual (p_i, τ_i) points $(i = 1, 2, \ldots)$:

$$v_i = \frac{1}{p_i},$$
$$z_i = \frac{1}{\varphi_i\,(p_{i+1})}\left[\tau_{i+1} - \sum_{j=1}^{i-1} z_j \varphi j\,(p_{i+1})\right], \tag{3}$$

where $z_i \geq 0$ is the thickness of the ith layer ($i \geq 0$), v_i is its velocity, and

$$\varphi_i\,(p) = \frac{2}{p v_i}\sqrt{1 - (p v_i)^2} \tag{4}$$

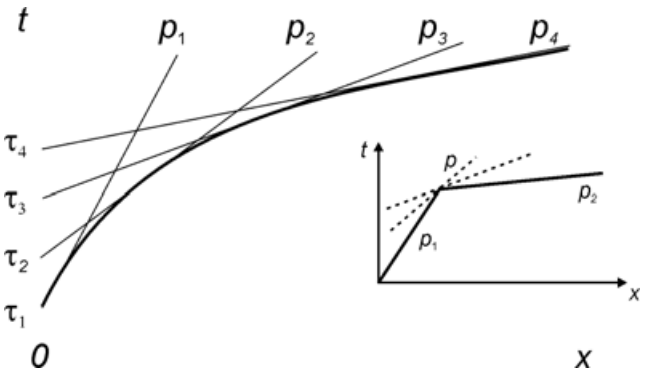

Figure 1. Approximation of a traveltime curve by an envelope of a suite of linear traveltime segments (head waves) $t(x) = \tau + px$. The inset shows the case of a velocity discontinuity, with an arbitrary set of layers with velocities $1/p$ (dashed lines; $p_1 > p > p_2$) hidden from the first arrivals by the deeper and faster layer.

is the intercept time per unit of layer depth. The parameters above are computed in a single pass from the top of the model to its bottom (Fig. 1), and the resulting stack of layers reproduces the traveltimes $\tau\ (p)$ exactly. If the value of τ_1 of the first $\tau\ (p)$ point is not zero (Fig. 1), the velocity v_0 of the uppermost layer has to be specified from additional considerations.

Two sources of errors influence the first-arrival inversion (2). First, the observed traveltimes can be approximated by the sequences of (p_i, τ_i) points in multiple ways. In particular, whenever a change of traveltime moveout is observed (and normally interpreted as being due to a velocity discontinuity), intermediate (p_i, τ_i) points can be introduced, with the corresponding head-waves hidden from the first arrivals (Fig. 1, inset; *cf.* Healy 1963). In such a case, inversion (1) would result in a set of velocity layers that are masked in the first arrivals by the underlying high-velocity layer. Secondly, even for smooth traveltime dependencies, different sampling sequences $\{p_i\}$ can approximate the original traveltimes to acceptable degrees, with each of them resulting in a significantly different velocity model.

Both of the above types of model uncertainties can be simulated by multiple inversions (3) with randomized (p_i, τ_i) parametrizations. Random realizations are generated by starting with a parametrization that is finely ($\delta p = 1 \times 10^{-4}$ s km^{-1}) and uniformly sampled in p_i and decimating it by randomly dropping (p_i, τ_i) points as long as the resulting piecewise-linear traveltime curve remains within the acceptable distance from all the data points (Fig. 2). In the IASP91 example, the acceptable traveltime misfit was taken 50 ms in the L_∞ (the maximum absolute value deviation) sense. The 50 ms L_∞ bracket was chosen as a very tight norm practically hardly attainable in regional-scale investigations, and amounting to only ∼0.02 per cent time errors (at ∼2000 km distances), and thus the resulting model variance should be due predominantly to the inversion null-space.

Note that dropping (τ, p) points from the convex traveltime IASP91 curve always results in traveltime delays (Fig. 2). Also, the scatter in $t(x)$ patterns changes sharply near 1670 km of offset (Fig. 2), corresponding to the depth of ∼120 km at which mantle velocity starts increasing (and, as the inversion shows, hidden layers become abundant, Fig. 3). The increased number of degrees of freedom below this depth leads to uneven sampling density of these areas in our random parametrization.

For a fixed $\{p_i, \tau_i\}$ parametrization, another type of model error arises from the possible low-velocity zones embedded within the layers. To explore this non-uniqueness, the model is also randomized by allowing a low-velocity zone of thickness $\gamma_i z_i$ and velocity $v_i(1 - \eta_i)$ near the bottom of each layer ($0 \leq \gamma_i \leq 1$ and $0 \leq \eta_i \leq 1$). The resulting depth model also accurately predicts the same traveltimes, provided its z_i are computed using eq. (3) with $\varphi_i(p)$ replaced with:

$$\tilde{\varphi}_i\,(p) = (1 - \gamma_i)\,\varphi_i\,(p) + \gamma_i \varphi_i\,[p\,(1 - \eta_i)]. \tag{5}$$

During this randomization, if solution (3) cannot be found for any given γ_i and η_i, these values are reduced and the inversion repeated until the value of z_i becomes positive.

INVERSION OF THE IASP91 FIRST-ARRIVAL TRAVELTIMES

To generate an ensemble of models that are close to IASP91 in the first-arrival sense, the randomizations and inversion (3) were repeated 200 times. The resulting suite of solutions shows significant scatter, in particular above the Moho and the 410 and 660 km discontinuities where the hidden layers are likely (Fig. 3a; Healy 1963). Note that the finest (undecimated) τ–p parametrization of

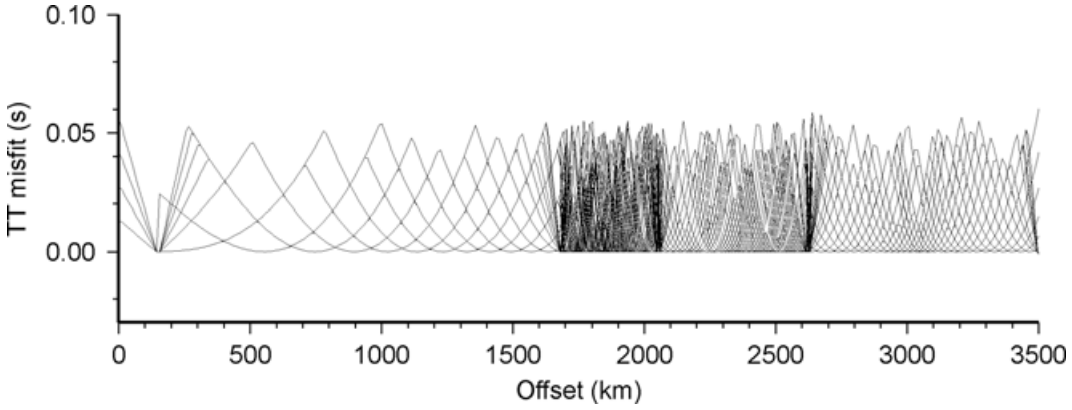

Figure 2. Traveltime misfits, relative to IASP91, of 50 (out of 200 generated) traveltime curves resulting from randomization of the regularly gridded $\tau_I(p_i)$ dependencies. Note that all the models lie within 0–50 ms from the IASP91 first-arrival traveltimes (the peak values slightly exceed 50 ms due to an approximate implementation of the L_∞ criterion) and thus they may be considered equally acceptable in terms of realistic first-arrival traveltime fit. Also note the change in density of sampling after ∼1670 km, as discussed in the text.

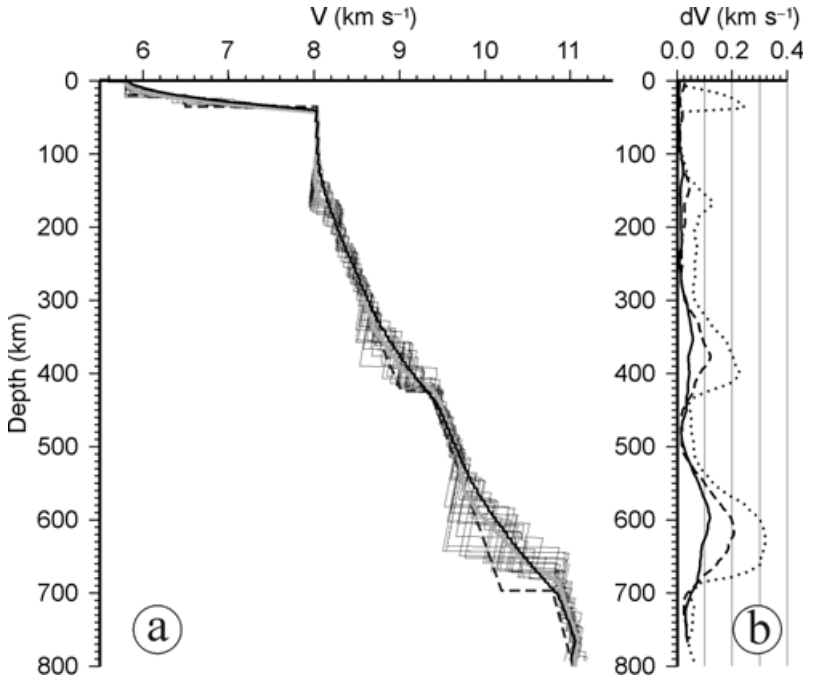

Figure 3. (a) 20 models out of our suite of 200 models (thin lines) with first-arrival traveltimes deviating IASP91 (dashed line) by no more than 50 ms (see Fig. 2), the smoothest (Herglotz–Wiechert) model (solid black line) and mean velocity (thick grey line); (b) velocity variance for three depth averaging scalelengths: no averaging (dotted line), 50 km (dashed line) and 100 km (solid line). Note that the velocity variance decreases with increasing depth averaging.

the IASP91 traveltime curve leads to a smooth model (the Herglotz–Wiechert solution) without first-order velocity discontinuities (black solid line in Fig. 3a). By allowing up to 5 per cent additional velocity decreases within half of the layer thickness ($\eta_i \leq 0.05$ and $\gamma_i \leq 0.5$ in eq. 5), we obtain yet stronger model uncertainty (Fig. 4).

Strong (∼2–3 per cent) velocity variations (Fig. 3), compared with ∼0.02 per cent perturbations of the traveltimes, suggest that the observed model variances are dominated by the null space ($\mathcal{M}_0$ in eq. 1). Repeating the above modelling with smaller, 10 and 30 ms L_∞ traveltime misfits confirms that the observed model scatter is nearly independent of data errors (Fig. 5).

From the standpoint of the first-arrival traveltime inversion, all the models in Figs 3 and 4 are equally acceptable within the chosen tight traveltime fit (Fig. 2). In particular, there is no reason to prefer the smoothest model, as it is actually one of the most dissimilar to the 'true' IASP91 velocity profile. An alternative to giving preference to a particular (constrained) inversion could be viewing the first-arrival inversion as only constraining a set of possible solutions that can be statistically characterized.

The attributes (statistics) used do describe the ensemble of possible models should include depth averaging. At almost any depth, velocities are widely scattered (Figs 3 and 4), and depth averaging would tighten their estimates. Also, only spatially averaged quantities are of significance for the interpretation of field refraction data. The depth-averaging scalelength is thus a free attribute of the model, and Figs 3(b) and 4(b) illustrate the dependence of velocity variance on this attribute. Note that the ensemble mean velocities are close to the Herglotz–Wiechert solution (only the mean values without depth averaging are shown in Fig. 2a). Velocity variances (Figs 3b and 4b) show strong trade-off with the averaging scalelength. Without

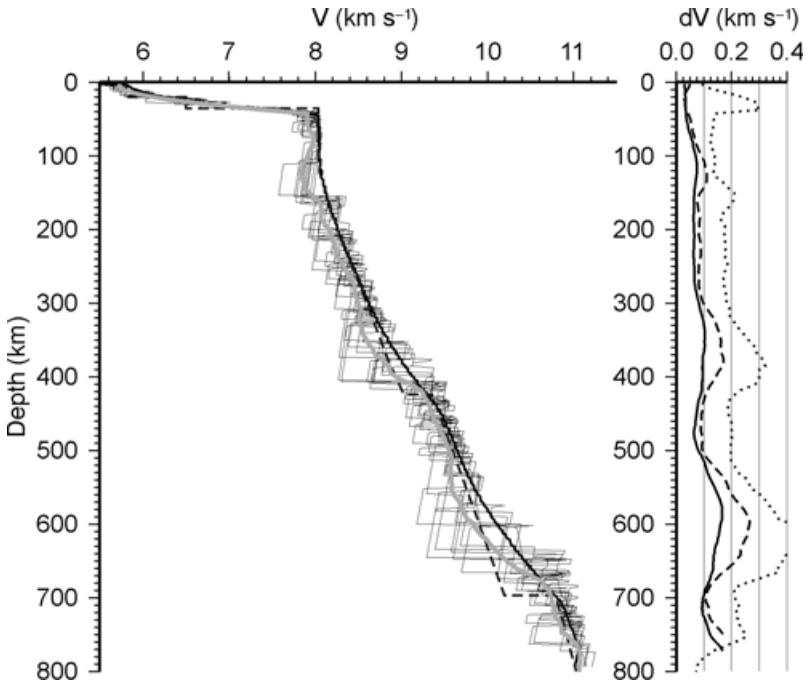

Figure 4. (a) 10 models out of 200 generated as in Fig. 3 but allowing 5 per cent low-velocity zones within each layer. (b) Velocity variance for these 200 models, using three averaging scalelengths as in Fig. 3.

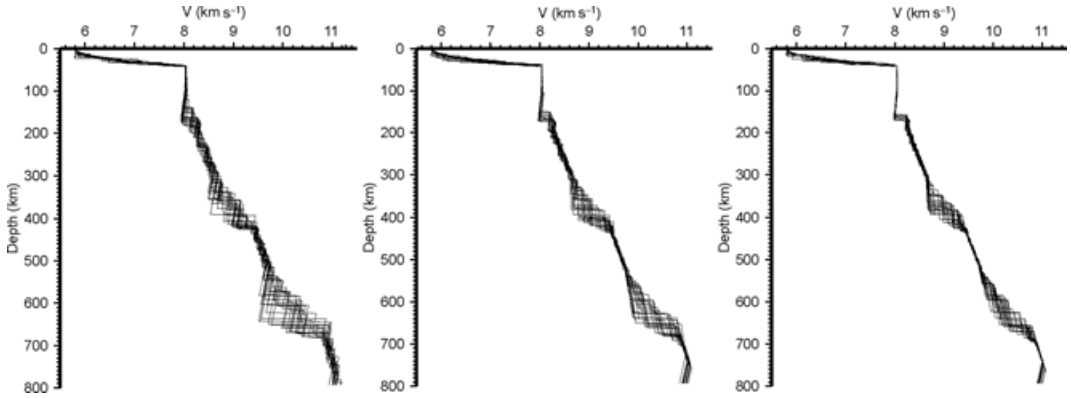

Figure 5. Ensembles of first-arrival traveltime models using 50-(Fig. 3), 30- and 10-ms L_∞ traveltime misfits. Although some sensitivity to data errors is present, the model distributions are close, suggesting that they are dominated by the null-space term in eq. (2).

averaging, velocity uncertainties above the Moho and both transition zone discontinuities are approximately 0.2 (Fig. 3b) or 0.3 km s^{-1} if low-velocity layers are considered (Fig. 4b), and drop to acceptable values of 0.1 km s^{-1} when 50 km depth averaging is applied (Fig. 3b). Note that as the velocity uncertainties increase above the discontinuities and near 160 km depth where the velocity gradient starts increasing (Fig. 3b), the optimal depth averaging could also be depth-dependent.

DISCUSSION

The statistical interpretation of first-arrival traveltime inversion implies that its results could only be interpreted in terms of ensemble- and depth-averaged velocity values. Spatial averaging is common to all geophysical measurements, and in seismics, this averaging is required primarily by wave phenomena. In ray-theoretical inversion, the finite-bandwidth effects can be approximated by simulating ray multipathing within Fresnel tubes (Yomogida 1992). For surface refraction first-arrival traveltimes, multipathing results in depth-velocity model uncertainties enhanced by layers hidden above the velocity discontinuities (Fig. 3) and particularly when moderate low-velocity sublayering is allowed (Fig. 4). The resulting models are thus sensitive to the procedures of their derivation and *a priori* constraints, and the statistical approach aims at characterizing this sensitivity.

The extents of the areas of velocity uncertainties caused by the discontinuities in Fig. 3 suggest heuristic scaling relationships useful for estimation of approximate depth-velocity uncertainties. Both the velocity δv) and depth extents (δz) of the scatter regions above a discontinuity (Fig. 3b) should be roughly proportional to the velocity contrast (Δv) across it, with δz also being inversely proportional to the average velocity gradient (of course, this approximation can be valid for positive velocity gradients only). By choosing the appropriate dimensionless constants to match the results in Fig. 3, we

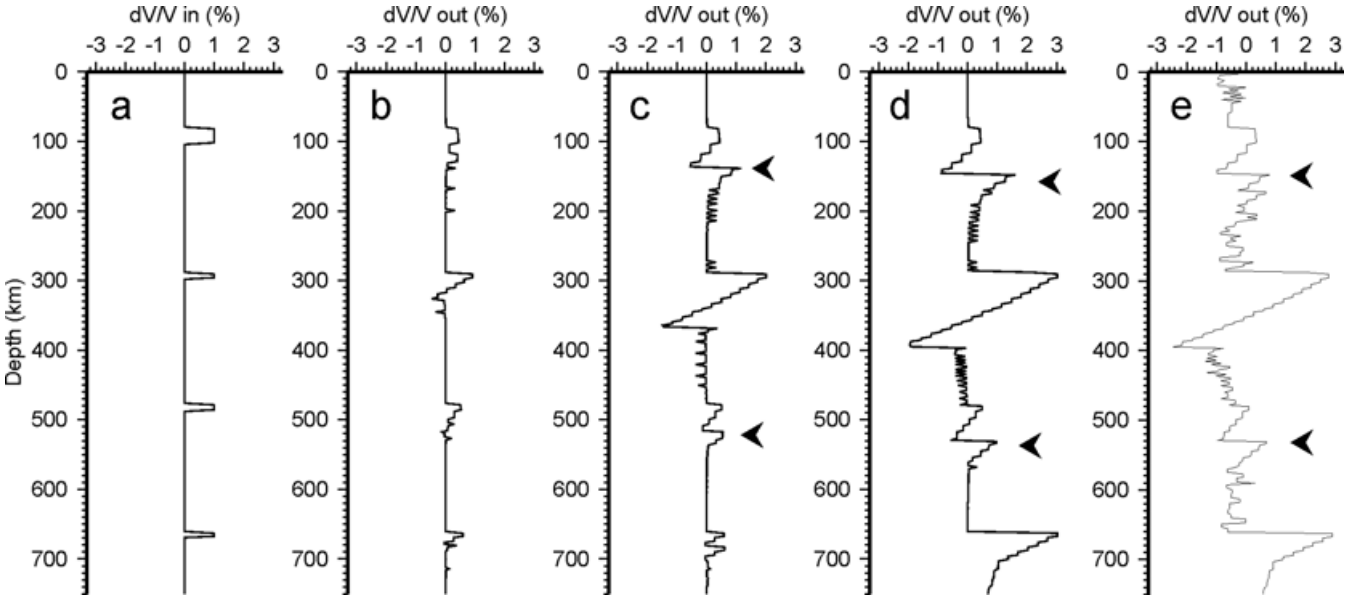

Figure 6. Resolution test by perturbing the velocities of four layers (indicated in a) in the model by: (b) 1 per cent, (c) 2 per cent, (d) 3 per cent, (e) 3 per cent, with 1 per cent contributions of stochastic low- velocity zones, as in Fig. 4. Note the dependence of resolution on the velocity gradient and perturbation amplitude. Arrows indicate the artefacts due to non-linearity of the inversion.

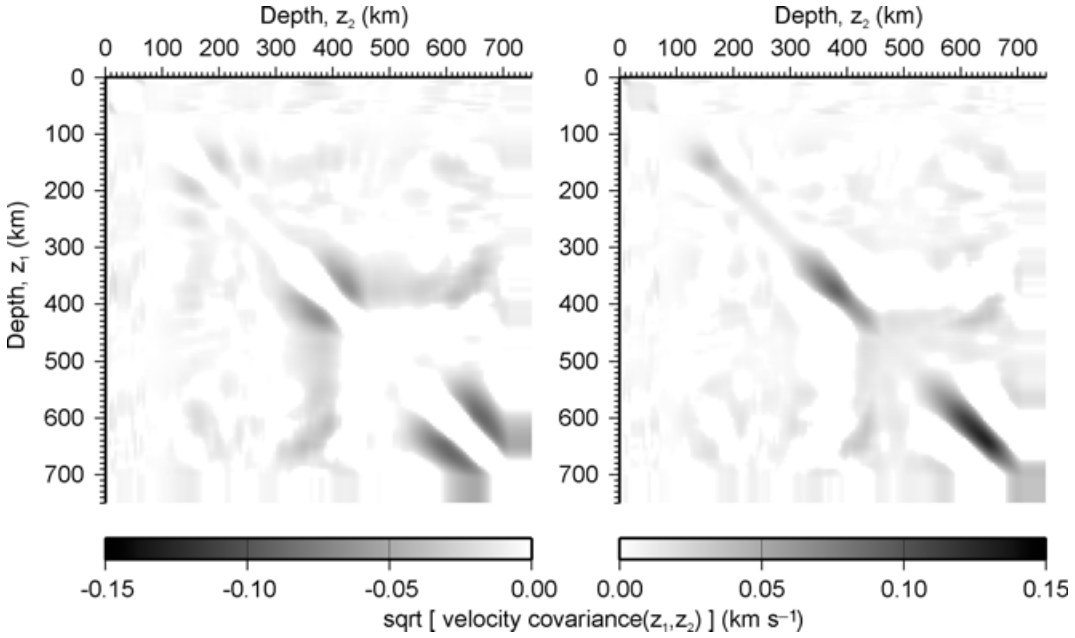

Figure 7. Velocity covariance matrix for the suite of models shown in Fig. 3 smoothed using a 50 km depth scalelength. Grey shading corresponds to the square root of the covariance: $\delta v(z_1, z_2) = \mathrm{sgn}[\mathrm{cov}(z_1, z_2)]\sqrt{|\mathrm{cov}(z_1, z_2)|}$. Left: negative covariances corresponding to anticorrelated velocity uncertainties; right: positive covariances. Note the extended off-diagonal regions of anticorrelated velocity uncertainties across the discontinuities. The background of patchy low-amplitude noise is due to a limited Monte Carlo sampling of the covariance.

estimate:

$$\delta v \approx 0.3\Delta v,$$
$$\delta z \approx 0.5\frac{\Delta v}{dv/dz}. \quad (6)$$

Hence, for an average crust ($\Delta v \approx 1$ km s^{-1} near the Moho, $dv/dz \approx 0.03$ s^{-1}; Christensen & Mooney 1995), the Moho would mask ~17 km of the lower crust from the first arrivals. The resulting velocity scatter would be of approximately 0.3 km s^{-1} that could be reduced by an appropriate choice of depth averaging (Fig. 3b). To account for these differences in the imaging environments of the upper and lower crust, depth-variant averaging and/or regularization could be used (Schueller *et al.* 1997).

Surface first-arrival traveltime inversion is both underconstrained and non-linear, and thus its results depend on the *a priori* constraints or algorithm parameters. Impulse-response resolution and variance estimates, such as the checkerboard tests commonly used in traveltime tomography, may significantly underestimate velocity uncertainties. These tests actually measure the linear response of the chosen inversion algorithm to data perturbations (the second term in eq. 2) and do not sample the null space.

To illustrate this problem, consider a 1-D impulse-response resolution test using 1, 2 and 3 per cent velocity increases (low-velocity layers of <3 per cent velocity contrasts are not reproduced at all) within selected layers followed by forward τ–p modelling and inversion (Fig. 6). As a result of the use of the regularized algorithm (without (τ p) decimation and resulting in the smooth solution in Fig. 3), velocity perturbations are reproduced reasonably well. However, the 2–3 per cent null-space velocity variance occurring (practically) without data perturbations (Figs 3–5) would overwhelm these responses. Thus, the ability of a regularized (i.e. ignoring the null-space) algorithm to resolve a particular model feature still does not mean that this feature can be unambiguously constrained from the data. Although described in 1-D, a similar null-space should also be present in greater dimensions.

The fidelity of reproduction of trial velocity perturbations (Fig. 6a) appears to be higher where the velocity gradients are stronger, whereas depth smearing is also increased in the same areas (Figs 6b–d). With ~2 per cent velocity perturbations, non-linear behaviour of the resolution matrix becomes apparent, and secondary lobes appear in low-gradient areas (marked with arrows in Figs 6c and d). The addition of 1 per cent, randomly distributed low-velocity zones (eq. 5) also introduces approximately 1 per cent of scatter into the resolution kernel (Fig. 6e). Since the multiparameter τ–p inversion (5) is relatively free from *a priori* constraints, these observations should relate to surface first-arrival inversion in general.

Reduction of the ensembles of alternative models to a set of depth-dependent summary attributes helps to visualize the depth dependence of the velocities and their uncertainties (Figs 3 and 4). However, such representation still does not reflect the null-space velocity covariances at different depth levels. For a selected depth-averaging scalelength, these covariances can be estimated through ensemble averages (denoted by $\langle\cdots\rangle$): $\mathrm{cov}(z_1, z_2) = \langle[v(z_1) - \langle v(z_1)\rangle][v(z_2) - \langle v(z_2)\rangle]\rangle$. Although covariances also represent only a part of the velocity trade-off in model (3), they reveal the dominant correlations between the velocities at different depth levels. Note that the velocities anticorrelate across the discontinuities in the IASP91 model (Fig. 7, left).

Both the smoothest and ensemble-mean solutions (thick curves in Fig. 3) suggest that first-order velocity discontinuities cannot be imaged from the first arrivals alone. Additional constraints, such as the maximum velocity gradients, reflections or partitioning of the model into layers including the positions of the associated cross-over points (Dobrin & Savit 1988) are needed to resolve the hidden layers above the discontinuities. Nevertheless, velocity variances (Fig. 3b) and covariances (Fig. 7) show correlations with the discontinuities in the true model—velocity variance increases above the discontinuities while the negative covariance is increased across them. Note that the 'true' IASP91 velocity profile could be loosely described as the low-velocity envelope of the distribution of the first-arrival models (Fig. 3). Velocity variance also increases in the areas of increased velocity gradients (near 130–180 km depth in Fig. 3), and thus it could be a good indicator of velocity and velocity gradient contrasts that may be less apparent from the individual inversions.

The discussion above showed that with *a priori* constraints relaxed, surface first-arrival inversion exhibits strong uncertainty that can be characterized statistically via Monte Carlo parameter testing. Re-evaluation of some of the existing interpretations may be required in order to estimate the extent and implications of this problem in inversions of real data. More tests are needed to refine the estimates (6) and to establish the character of velocity uncertainties in 2- and 3-D cases. Reflections add critical constraints to traveltime interpretations; however, even with reflection traveltimes included, significant uncertainties caused by hidden (including the low-velocity) layers still remain.

CONCLUSIONS

Null-space of surface first-arrival inversion has a major impact on the resulting model variance, as illustrated on the example of 1-D IASP91 model. Although in a checkerboard test, regularized inversion appears to reproduce positive velocity perturbations adequately; null-space velocity fluctuations exceed these responses in many cases of interest. Consequently, the amount of model detail recoverable from the data by regularized and linearized tomography may be overestimated. In contrast, non-linear, unconstrained, Monte Carlo inversion allows quantitative assessment of the full model variance, including the null-space contribution. Velocity variances trade off with the depth averaging scalelength and depend on the velocity structure, with increasing variances above velocity discontinuities. Although velocity discontinuities cannot be established from a single unconstrained inversion of the first-arrival traveltimes, they can be associated with the zones of increased velocity variance. The results derived for 1-D should remain applicable to the first-arrival traveltime inversion in higher dimensions.

ACKNOWLEDGMENTS

This research was performed at the University of Wyoming Reflection Seismology Laboratory. Comments by Scott Smithson, Robert Nowack, Colin Zelt and Associate Editor Steven Ward have greatly helped in improving the manuscript. This work was sponsored by the Defence Threat Reduction Agency Grants DSWA01-98-0015, DTRA01-00-C-031 (subcontract from Columbia University), and DTRA01-01-C-0057.

REFERENCES

Aki, K. & Richards, P.G., 2002. *Quantitative Seismology,* 2nd edn, University Science Books, Sausalito.

Bessonova, E.N., Fishman, V.M., Ryaboy, V.Z. & Sitnikova, G.A., 1974. The tau method for inversion of traveltimes, 1, Deep seismic sounding data, *Geophys. J. R. astr. Soc.*, **36,** 377–398.

Buland, R. & Chapman, C.H., 1983. The computation of seismic travel times, *Bull. seism. Soc. Am.*, **73,** 1271–1302.

Christensen, N.I. & Mooney, W.D., 1995. Seismic velocity structure and composition of the continental crust: a global view, *J. geophys. Res.*, **100,** 9761–9788.

Healy, J.H., 1963. Crustal structure along the coast of California from seismic-refraction measurements, *J. geophys. Res.*, **68,** 5777–5787.

Kennett, B.L.N. & Engdahl, R., 1991. Traveltimes for global earthquake location and phase identification, *Geophys. J. Int.* **105,** 429–465.

Menke, W., 1989. Geophysical data analysis: discrete inverse theory, p. 289 Academic, San Diego.

Pavlenkova, N.I., 1982. The intercept-time method: possibilities and limitations, *J. Geophys.,* **51,** 85–95.

Pullammanappallil, S.K. & Louie, J.N., 1994. A generalized simulated-annealing optimisation for inversion of first-arrival times, *Bull. seism. Soc. Am.*, **84,** 1397–1409.

Schueller, W., Morozov, I.B. & Smithson, S.B., 1997. Crustal and uppermost mantle velocity structure of northern Eurasia along the profile QUARTZ, *Bull. seism. Soc. Am.*, **87,** 414–426.

Yomogida, K., 1992. Fresnel zone inversion for lateral heterogeneities in the Earth, *Pure appl. Geophys.*, **138,** 391–406.

Zelt, C.A., 1999. Modelling strategies and model assessment for wide-angle seismic traveltime data, *Geophys. J. Int.* **139,** 183–204.

Zhang, J. & Toksőz M.N., 1998. Nonlinear refraction traveltime tomography, *Geophysics*, **63,** 1726–1737.